Supplementary Information

Janus biocomposite aerogels constituted of cellulose nanofibrils and MXenes for application as single-module solar-driven interfacial evaporators

Xinhong Han,[a] Shaoqiu Ding,[a] Liwu Fan,[a] Yonghao Zhou [a] and Shurong Wang *[a]

[a] State Key Laboratory of Clean Energy Utilization, Zhejiang University, Hangzhou 310027, P. R. China. E-mail: srwang@zju.edu.cn

Supporting Notes

Note S1. Density and porosity evaluation

The apparent density (ρ_{app}) of the aerogels was calculated as follows:

$$\rho_{app} = \frac{m}{V}$$

where m and V indicate the weight and volume of the aerogels, respectively.

The porosity was calculated based on the following equation:

$$porosity = \left(1 - \frac{\rho_{app}}{\rho_s}\right) \times 100\%$$

where ρ_s denotes the real density of solid framework, calculated according to the following equation:

$$\rho_s = \frac{1}{\dfrac{\omega_{CNF}}{\rho_{CNF}} + \dfrac{\omega_{MXene}}{\rho_{MXene}} + \dfrac{\omega_{poly(MTMS)}}{\rho_{poly(MTMS)}} + \dfrac{\omega_{ECH}}{\rho_{ECH}}}$$

where ω_{CNF}, ω_{MXene}, $\omega_{poly(MTMS)}$, ω_{ECH} are the weight fractions of each component; ρ_{CNF}, ρ_{MXene}, $\rho_{poly(MTMS)}$, ρ_{ECH} are the true densities of each component; ρ_{CNF}, ρ_{MXene}, $\rho_{poly(MTMS)}$, and ρ_{ECH} were taken as 1500 kg m⁻³,[1–3] 3800 kg m⁻³,[4] 1900 kg m⁻³,[1] and 1180 kg m⁻³, respectively.

Note S2. Numerical simulation of temperature distribution in JCM aerogels

Numerical heat transfer simulation was conducted using COMSOL Multiphysics 5.3 under transient analysis mode. The 2D microstructural model was built as shown in Figure S9a, where the well-aligned microchannels were simulated as parallel rectangles with widths of 86, 28, and 56 μm, according to the SEM images. Calculation of non-isothermal flow was conducted by introducing the multiphysics of laminar flow coupled with solid and liquid heat transfer, ignoring the curvature of the microchannels and the deformation of the skeleton owing to absorption/flow of water. The solar irradiation input at the top was considered as a constant

heat flux of 1000 W m^{-2} consistent with the simulated sunlight intensity in the experiment. It was assumed that the initial temperature of the skeleton and liquid was 20 °C, and there were thermal insulation boundaries on both sides. The heat transfer of the fluid in the microchannels was regarded as internal natural convection, and the velocity field obtained by laminar flow calculation was used as the convective heat transfer velocity. Thermal radiation at the top was also considered, and the emissivity and ambient temperature were set to 0.9 and 20 °C, respectively. Water evaporation was assumed to occur on the surface of the solid wall, and the vaporization enthalpy was regarded as the boundary heat source.

The heat transfer simulation estimated maximum temperature of the model surface to be 59 °C (Figure S9b), which is close to the experimental value. The temperature changes mainly occurred in the region near the upper surface, which indicated that most of the heat was stored there. As the thermal conductivity of JC10M5 is low, and part of the heat transferred downward would have been absorbed by the water in network channels, the temperature of the lower surface was estimated to be nearly the same as the initial temperature. The transient analysis results showed that only the temperature at the top increased in the initial stage (t=0 s), and heat was gradually transferred to the interior of the aerogel (t=1 s) owing to the dynamic balance between the continuous heat input by sunlight and water evaporation-induced heat consumption (Figure S9b and c). Since the size of the microscopic model is three orders of magnitude smaller than that of the actual JC10M5, the top evaporation surface temperature of the micro model reached a nearly stable value within 1 s. As shown in Figure S9d, the temperature of the skeleton is slightly higher than that of the fluid region, and this phenomenon is more obvious near the

bottom.

To obtain a comprehensive understanding of the temperature changes of the actual aerogels, we also conducted a simulation on the 3D macroscopic model. The overall temperature distribution of the model containing JC10M5 and the bulk water at the 4th hour can be clearly observed from Figure S10. The surface temperature reached dynamic equilibrium in about 2 minutes and was maintained at 57 °C, which was almost consistent with the results of the 2D simulation and the experiment. At the interface between JC10M5 and the bulk water, the temperature increased slowly within 4 hours, and the rising trend was faster in the first hour (from 20 °C to 25 °C) than that in the next three hours (from 25 °C to 31 °C). The heat mainly concentrated in the upper part, indicating the good temperature management of JC10M5.

Note S3. Numerical simulation of water transport in JCM aerogels

Numerical mass transfer simulation was conducted using COMSOL Multiphysics 5.3. The outflow boundary condition was set to a normal outflow velocity of 2.29 kg m^{-2} h^{-1} (6.36×10^{-7} m s^{-1}) and free flow condition was considered at the bottom. Because a no-slip wall was assumed, the fluid velocity near the wall was zero. The model depicted the ideal state of water transfer, ignoring the water penetration in the skeleton. The water transport simulation estimated the maximum transport velocity to be 9.76×10^{-7} m s^{-1} (~3.51 kg m^{-2} h^{-1}), and that the average value could reach 6×10^{-7}–7×10^{-7} m s^{-1} (2.16–2.52 kg m^{-2} h^{-1}), which is in good agreement with the experimental results. As shown in the map of the water transport velocity distribution (Figure S11), water was being continuously removed by evaporating at the upper surface, while steady-state water transport upwards through the channels offset the amount of

water evaporated. From 0 s to 1 s, the vapor transport became stable and continuous, and the maximum velocity was gradually concentrated in the center of the channels, which might be due to the formation of a thin water film on the channel wall, resulting in a lower velocity near the wall.
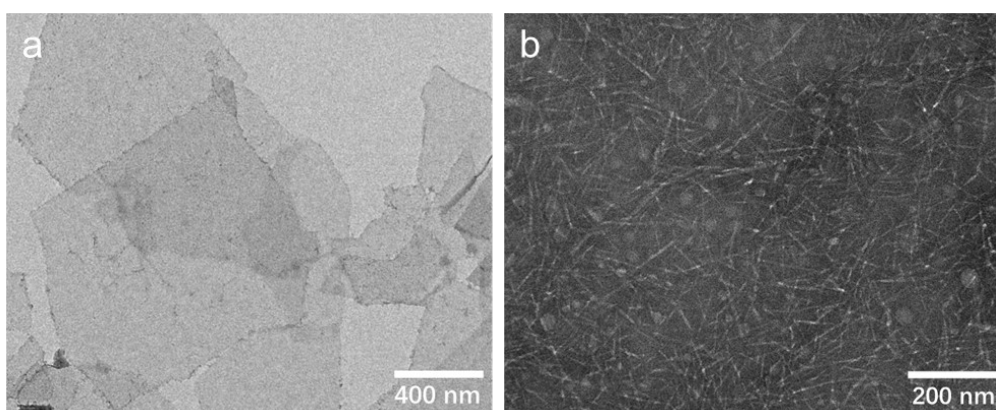
Supporting Figures

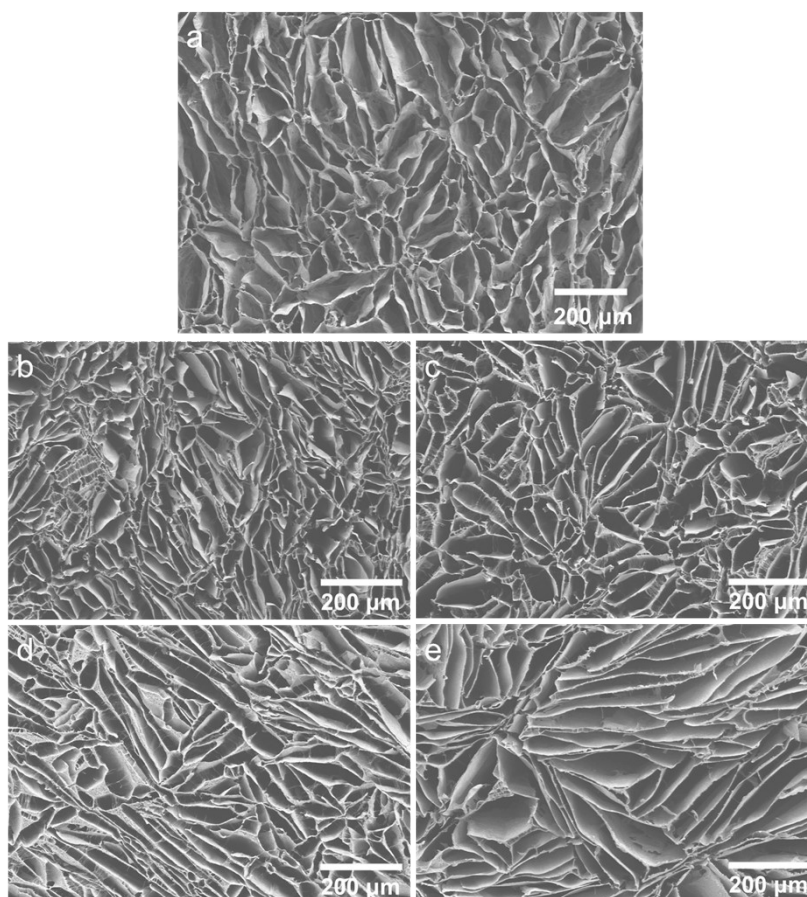**Figure S1**. TEM images of (a) $Ti_3C_2T_x$ MXene nanosheets and (b) CNFs.

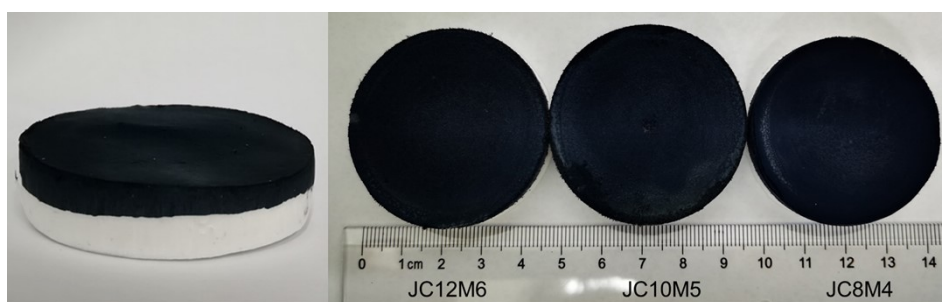**Figure S2.** SEM images of (a) CA, (b) C11M4, (c) C9M6, (d) C8M4, and (e) C12M6.

Figure S3. Digital photographs of JCM aerogels.
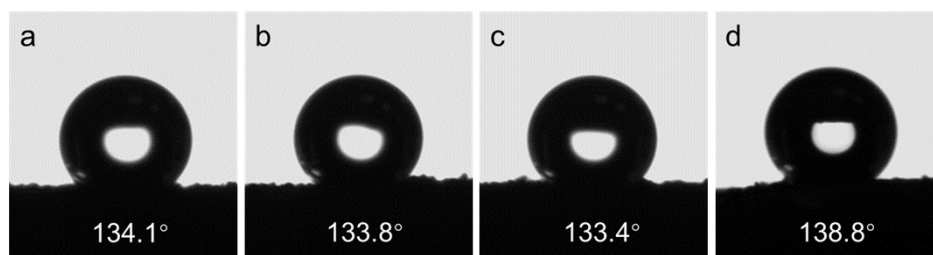
Figure S4. Water contact angle images on the surface of (a) C8M4, (b) C12M6, (c) C11M4, and (d) C9M6.
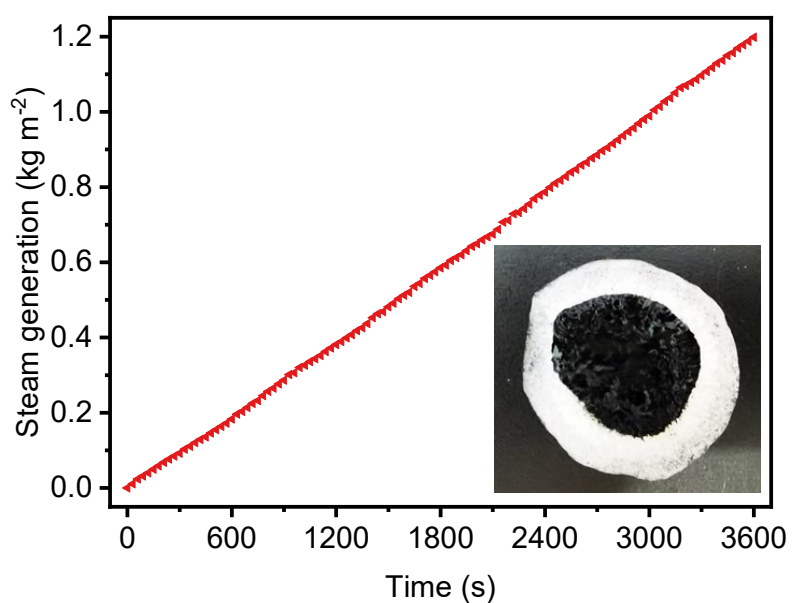

Figure S5. Generation of water vapor over time using the sample without MTMS modification (with 10 g L^{-1} CNFs and 5 g L^{-1} MXenes in the precursor of the upper layer) under one sun; the inset image is the digital photograph of the sample after absorbing water.
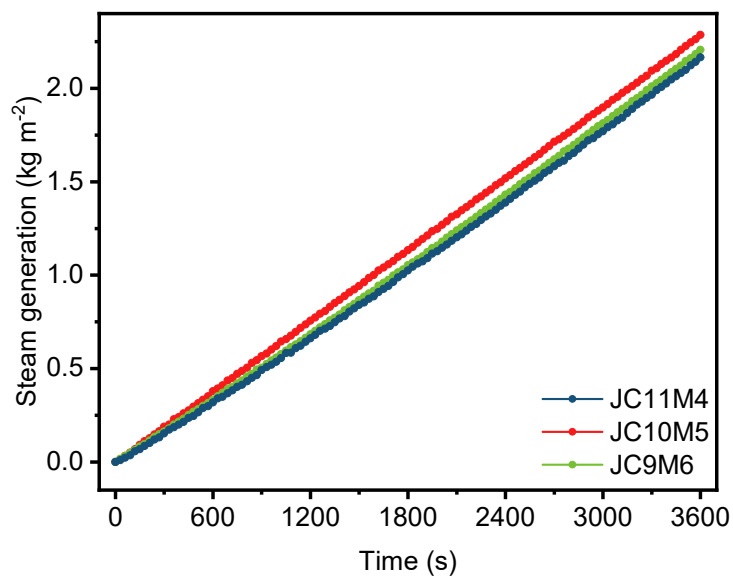
Figure S6. Generation of water vapor over time by JCM aerogels with different CNF/MXene weight ratios under 1 sun.
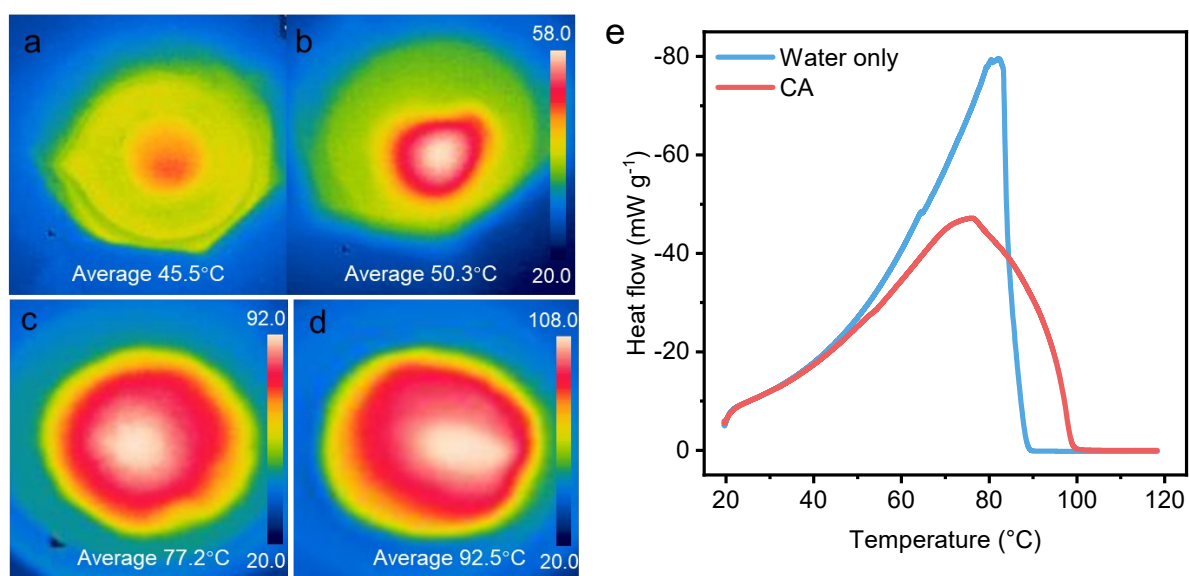

Figure S7. Infrared images of the upper surface of (a) JC11M4 under 1 sun, (b) JC9M6 under 1 sun, (c) JC10M5 under 2 suns, and (d) JC10M5 under 3 suns. (e) Thermograms of CA hydrogel and pure water tested by DSC.
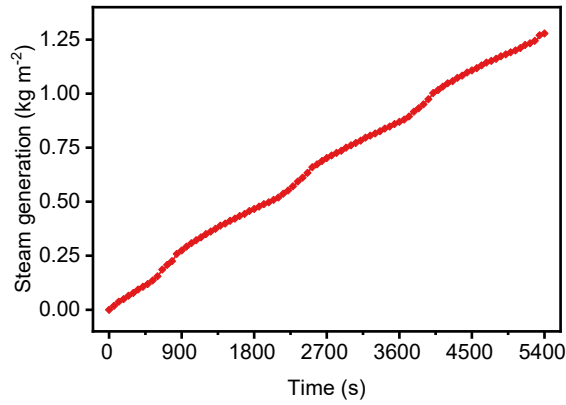
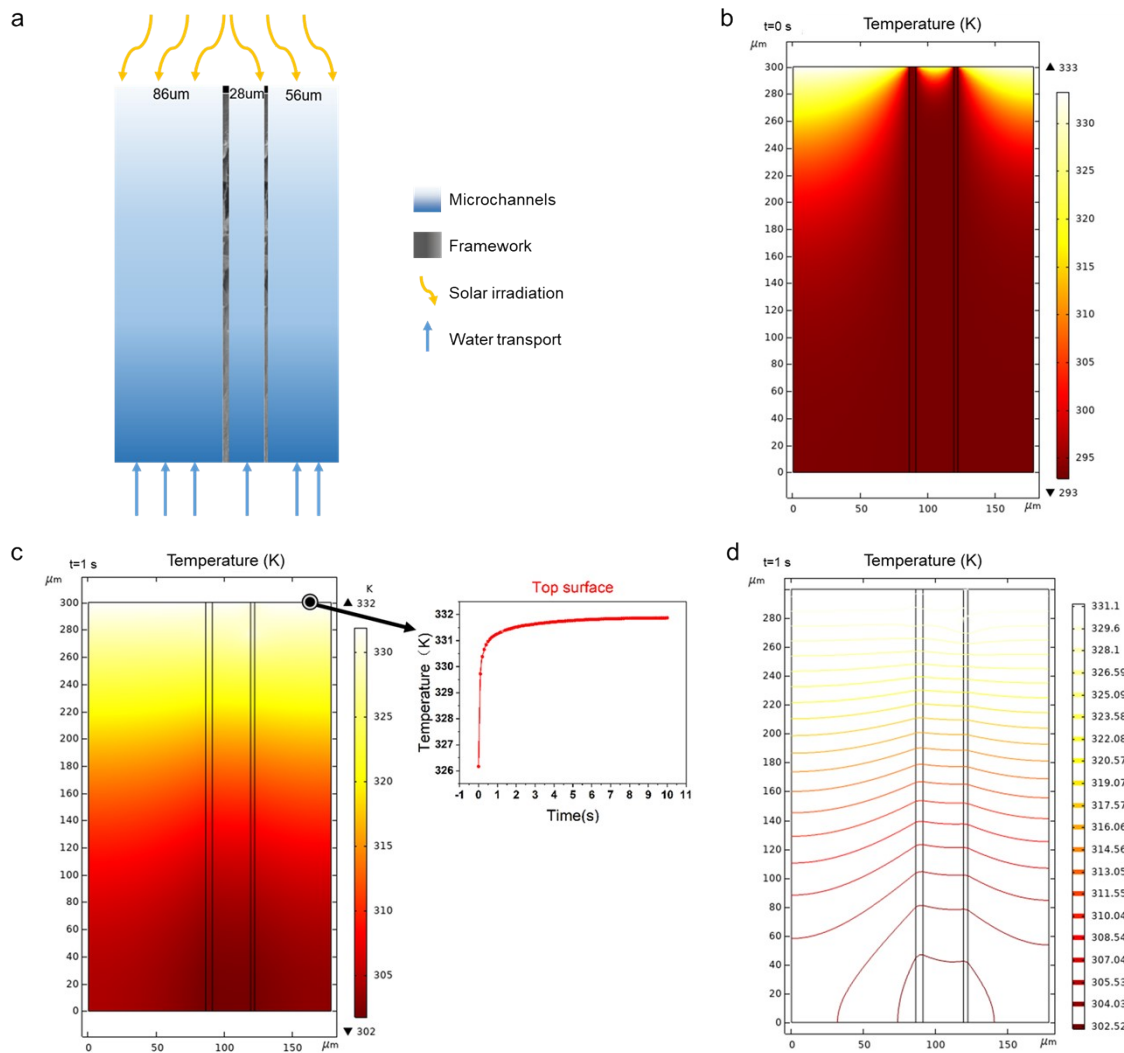**Figure S8.** Generation of water vapor over time by JC10M5 in the dark.

Figure S9. (a) 2D Microstructural model of JC10M5. (b) Temperature distribution in JC10M5

at 0 s. (c) Temperature distribution in JC10M5 at 1 s, and the curve of surface temperature

9

versus time. (d) Temperature distribution in JC10M5 at 1 s (visualized in the form of isotherm).
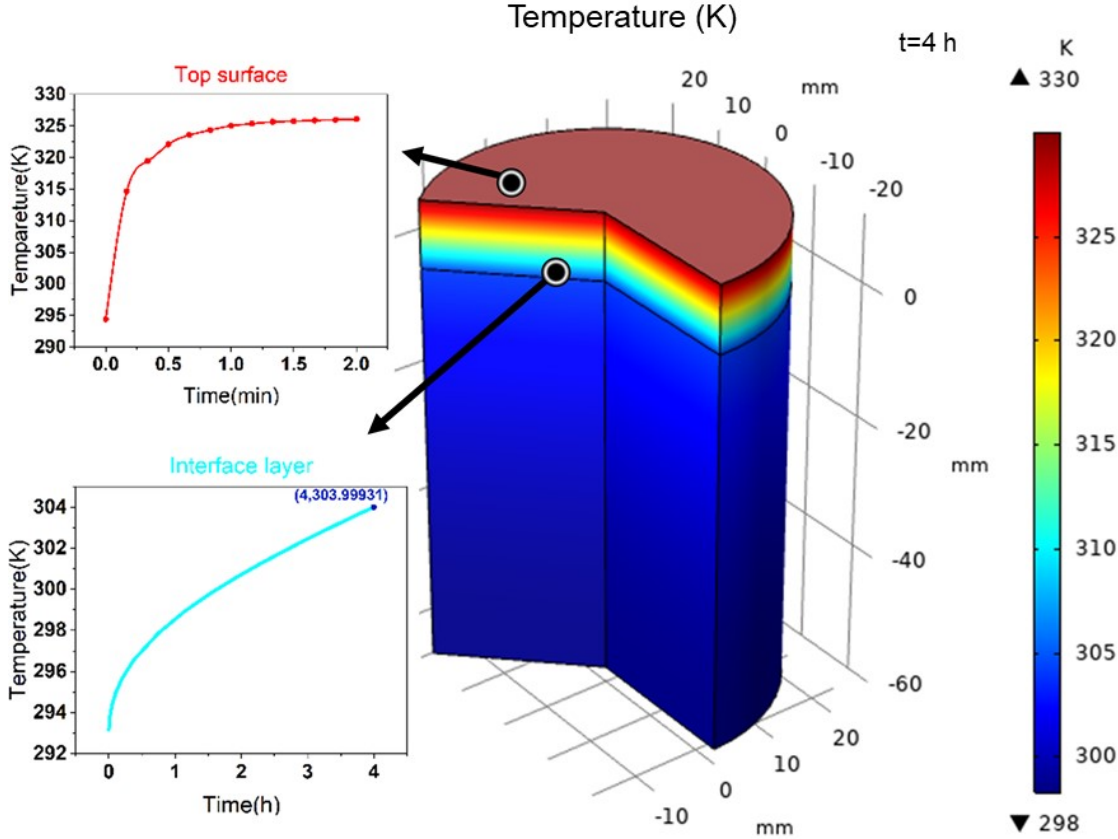

Figure S10. Temperature distribution for the 3D macrostructural model of JC10M5 and bulk

water at the 4th hour, and the curves of temperature versus time at the top surface of JC10M5

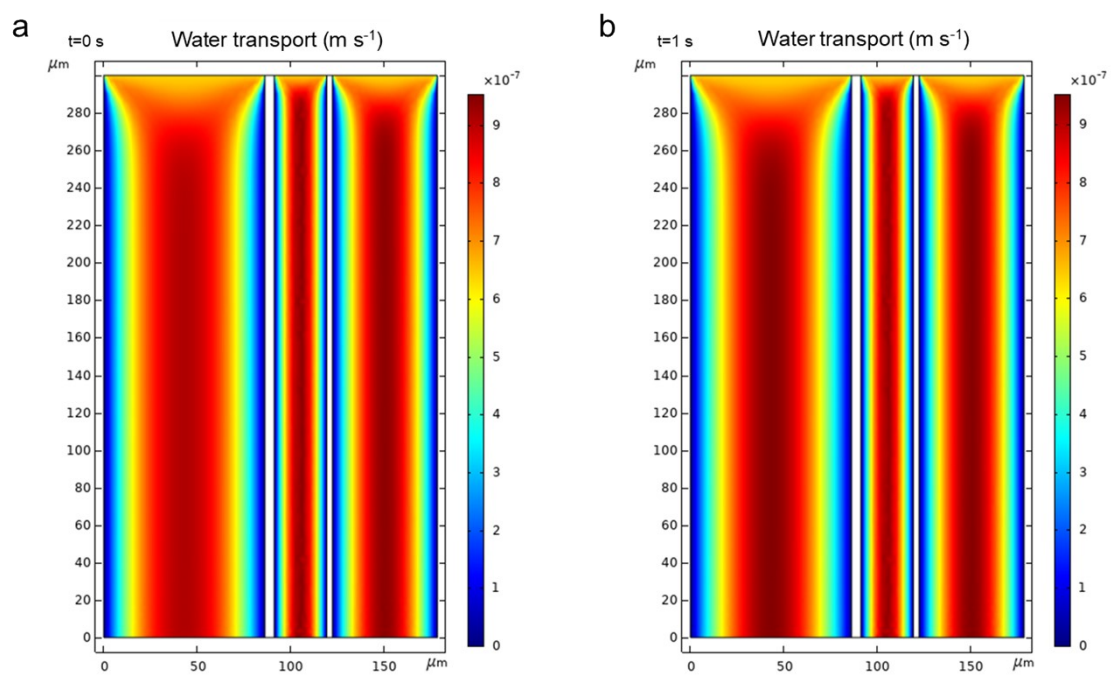and the interface between JC10M5 and bulk water.

Figure S11. Results of numerical simulation for water transport velocities in JC10M5 at (a) 0 s and (b) 1 s.
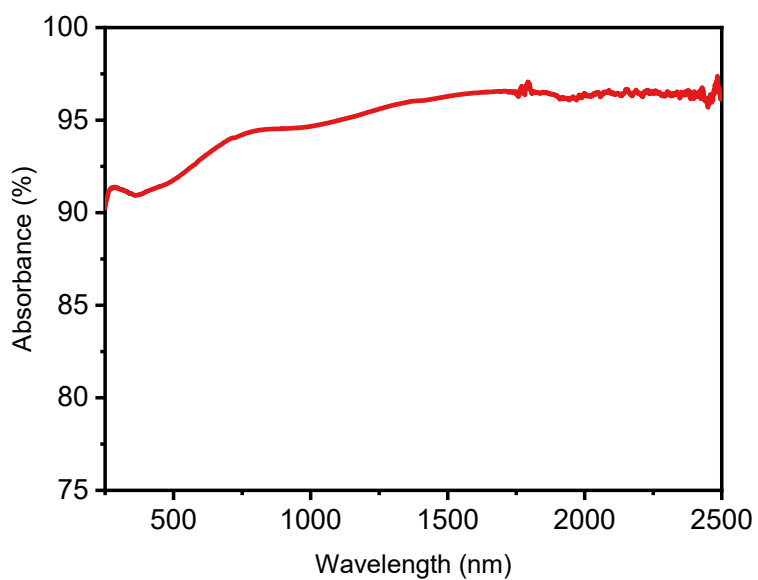

Figure S12. UV-vis-NIR absorbance spectrum of JC10M5 after evaporating 3.5 wt% NaCl solution under 1 sun for 10 days (6 h a day).
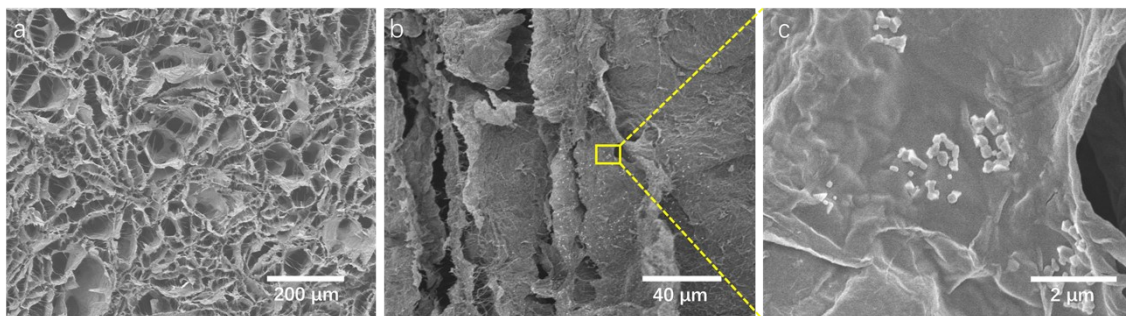
Figure S13. SEM images of the upper part of JC10M5 after evaporating 3.5 wt% NaCl solution under 1 sun for 10 days (6 h a day). (a) Cross-section. (b-c) Longitudinal section.

Figure S14. Digital photograph of the simulated seawater desalination device.

Supporting Tables

Table S1. Apparent densities and porosities of the aerogel samples.

	C11M4	C10M5	C9M6	C8M4	C12M6	CA
Apparent density (kg m^{-3})	21.41	21.37	21.04	20.73	23.92	18.28
Porosity (%)	98.67	98.70	98.75	98.74	98.54	98.67

Table S2. Axial and radial thermal conductivities of CM aerogels and the CA saturated with water.

	C11M4	C10M5	C9M6	C8M4	C12M6	Wetted CA
Axial thermal conductivity (W m^{-1} K^{-1})	0.05743	0.04445	0.04174	0.04585	0.05459	0.53136
Radial thermal conductivity (W m^{-1} K^{-1})	0.02495	0.02812	0.03867	0.02843	0.03288	0.49585

Table S3. DSC results.

	CA hydrogel	Pure water
Total mass (mg)	11.30	12.12
Water (mg)	11.06	12.12
Enthalpy (J g^{-1})	2071	2204

Table S4. Calculation details of evaporation efficiency.

	P_{in} (kW m^{-2})	$\dot{m}$ (kg m^{-2} h^{-1})	h_{LV} (kJ kg^{-1})	η (%)
JC10M5	1	1.442	2202.04	88.2
JC10M5	2	2.355	2311.24	75.6
JC10M5	3	3.084	2375.50	67.8
JC11M4	1	1.308	2178.1	79.1
JC9M6	1	1.446	2205.82	88.6
JC8M4	1	1.355	2180.20	82.1
JC12M6	1	1.460	2210.86	89.7

References

1. Z. Zhang, G. Sèbe, D. Rentsch, T. Zimmermann and P. Tingaut, *Chemistry of Materials*, 2014, **26**, 2659-2668.

2. T. Wu, Z. Zeng, G. Siqueira, K. De France, D. Sivaraman, C. Schreiner, R. Figi, Q. Zhang and G. Nyström, *Nanoscale*, 2020, **12**, 7383-7394.

3. H. Sehaqui, M. Salajková, Q. Zhou and L. A. Berglund, *Soft Matter*, 2010, **6**, 1824-1832.

4. M. Ghidiu, M. R. Lukatskaya, M.-Q. Zhao, Y. Gogotsi and M. W. Barsoum, *Nature*, 2014, **516**, 78-81.